J. Iron Steel Res. Int. (2019) 26:173–181
https://doi.org/10.1007/s42243-018-0213-1

ORIGINAL PAPER

Deformation behavior and microstructural evolution in ultra-high-strength dual-phase (UHS-DP1000) steel with different strain rates

Mei Xu[1] · Hui Li[2] · Rui-ting Jiang[1] · Di Tang[3] · Hai-tao Jiang[1] · Zhen-li Mi[1]

Received: 8 October 2017 / Revised: 8 November 2017 / Accepted: 20 November 2017 / Published online: 5 January 2019

Abstract
The dynamic tensile behavior and deformation mechanism of ultra-high-strength dual-phase (UHS-DP1000) steel were investigated over a wide range of strain rates from 10^{-4} to 10^{3} s^{-1}. As the strain rate increases, the transition strain decreases from 2.73 to 1.92, and the martensite plastic deformation starts earlier. At strain rate of 10^{-4}–0.5 s^{-1}, the inhomogeneous plastic deformation ability increases because the dislocation density in the ferrite matrix increases. This leads to a decrease in uniform elongation and an increase in fracture elongation. When the strain rate increases from 0.5 to 500 s^{-1}, the amount of mobile dislocation increases, which is the main reason for the enhancing uniform elongation and fracture elongation. Meanwhile, because the dislocation motion resistance rapidly increases, the yield strength and ultimate tensile strength also increase. When the strain rate is higher than 500 s^{-1}, the hardening behavior caused by the dislocation motion resistance has not been offset by softening due to the mobile dislocation and adiabatic heating. The voids at the early stage of deformation could not uniformly form and grow, and thus the homogeneous plastic deformation ability decreases.

Keywords Ultra-high-strength dual-phase steel · Strain rate · Microstructural evolution · Void · Adiabatic heating

1 Introduction

The use of lightweight materials, which promote energy conservation and emission reduction, is the main method adopted by the automobile industry to address the challenges of environmental pollution and energy shortages. The exploitation and application of advanced high-strength steel (AHSS) have become a new means to this end [1, 2]. The ferrite/martensite dual-phase (DP) steel is a representative of AHSS [3]. Previous studies have confirmed that DP steels possess a low yield ratio of stress to ultimate strength, high initial work hardening rate, good formability and high energy-absorption capability. These characteristics allow them to meet the requirements of the automotive industry such as mass reduction and crashworthiness [4–6].

In the preceding research on DP steel, the microstructure, manufacturing process, strain hardening behavior and deformation mechanism have usually been studied under quasi-static tensile tests. Mazaheri et al. [7] reported the effects of intercritical annealing temperature on the microstructural evolution and mechanical properties. The variations in hardness, strength, elongation, strain hardening behavior and fracture mechanism of the specimens with intercritical annealing temperature are all included in this study. Zhao et al. [6] investigated the influences of different annealing temperatures on the mechanical properties of an ultra-high-strength (UHS) DP steel. They found that as the intercritical annealing temperature increased, martensite coarsened and tempered at some high degree, and the ferrite volume fraction decreased observably. Rao et al. [8] analyzed the work hardening behavior of the ultrafine-grained (UFG) DP steels, and their results show a continuously varying work hardening rate response that could be approximated by two or three linear regimes.

✉ Zhen-li Mi
zhenli_mi@163.com

[1] Institute of Engineering Technology, University of Science and Technology Beijing, Beijing 100083, China

[2] College of Engineering, Yantai Nanshan University, Yantai 265700, Shandong, China

[3] Collaborative Innovation Center of Steel Technology, University of Science and Technology Beijing, Beijing 100083, China

Tomita and Okabayashi [9] mentioned that the modified Crussard-Jaoul (C-J) was the most suitable model for describing the work hardening of DP steels. Their results reveal that there are two-stage work hardening characteristics. The first stage is associated with the deformation of the ferrite matrix, and the second stage is associated with the uniform strain of the ferrite and martensite.

In addition, previous studies also reveal that compared with the quasi-static state, there are significant differences in mechanical properties and deformation behavior under dynamic loading. Beynon et al. [10] found that as the strain rate increased from 10^{-3} to 10^{2} s^{-1}, the strength was enhanced and the strain hardening rate decreased in DP500 and DP600 steels. Curtze et al. [11] reported the yield strength (R_e) and ultimate tensile strength (R_m) increased slowly at strain rates from 10^{-3} to 1250 s^{-1} for DP600 steel. Cai et al. [12] investigated the dynamic mechanical behavior and constitutive model of DP800 steel under strain rates of 500, 1000 and 2250 s^{-1}. Yu et al. [13] proposed a plastic flow law on the basis of the Johnson–Cook rate-dependent constitutive model at the strain rates from 10^{-4} to 1600 s^{-1} for DP600 steel. The constitutive model could perfectly describe the mechanical behavior at low and high strain rates. Oliver et al. [14] performed dynamic tensile test at low and high strain rates within the range of 0.001–200 s^{-1} for DP(600–800) steels and transformation-induced plasticity TRIP(600–1000) strip steels. They found that, with increasing strain rate, the strength and energy absorption increased for all the steel grades, but the work hardening exponent decreased. The aforementioned results indicate that the mechanical properties of DP steel are sensitive to the strain rate. These studies have ignored the micromechanism of deformation at different strain rates. However, it is very important to confirm the effect of strain rate on the deformation mechanism for DP steel because it, especially for the UHS-DP steel, is usually used in safety structures. Therefore, the aim of this study is to further understand the effect of strain rate on the deformation micromechanism for UHS-DP1000 steel with a typical duplex microstructure. The mechanical properties were tested under quasi-static and dynamic loading tensile experiments over a wide range of strain rates from 10^{-4} to 10^{3} s^{-1}. The strain hardening behavior was analyzed at different strain rates based on the modified C-J analysis, and the effects of strain rate on the microstructural features, dimple fracture characteristics and void evolution were also discussed.

2 Experimental procedure

The UHS-DP1000 steel used in this study was melted in a vacuum induction melting furnace under argon atmosphere. The exact chemical composition is listed in Table 1. The ingots were forged into several billets with dimensions of 40 mm × 80 mm × 90 mm, which were then homogenized at 1200 °C for 2 h and subjected to seven-pass hot rolling in the temperature range of 900–1200 °C. The hot-rolled steels with a final thickness of 4 mm were cold-rolled to a thickness of 1.2 mm. Subsequently, the cold-rolled steels were reheated to the annealing temperature of 880 °C, followed by isothermal holding for 10 min. Then, the annealed steel plates were cut into dog-bone tensile samples with a gauge length of 20 mm along the rolling direction using a wire cutting machine.

Quasi-static and low rate tests at the strain rates of 10^{-4}, 10^{-3}, 10^{-2} and 10^{-1} s^{-1} were carried out using a CMT5105 tensile test machine, and dynamic tests at the strain rates of 10^{0}, 10^{1}, 10^{2}, 5×10^{2} and 10^{3} s^{-1} were performed on a Zwick HTM16020 high-speed tensile test machine. All the tensile tests were conducted at room temperature, and five tensile samples were tested at each strain rate. Compared with the samples used in quasi-static tests (i.e., low strain rate tensile tests, 111 mm), the total length of the dynamic samples is 280 mm in order to obtain a constant tensile velocity, whereas the gauge length is the same. The gauge width is 10 mm for all the specimens. Optical microscope (OM, ZEISS AX10), transmission electron microscope (TEM, JEOL JEM 2000 FX) and field emission scanning electron microscope (FE-SEM, FEI 450) were used to characterize the microstructure and the fracture morphology. The TEM specimens were prepared by mechanical grinding to a thickness of 50 μm and electro-polishing with a twin jet electro-polisher at − 15 °C using a solution containing 85 vol.% C_2H_5OH and 15 vol.% $HClO_4$.

In addition, the tensile curves under the dynamic tests show significant fluctuation. Therefore, the engineering stress–strain curves obtained from the Zwick HTM16020 high-speed tensile test machine were first moved left to eliminate the high-frequency signals and then smoothed using the adjacent-averaging method in the OriginPro data processing software.

3 Results and discussion

3.1 Microstructure before deformation

The initial microstructure of experimental UHS-DP1000 steel (Fig. 1) exhibits a typical duplex microstructure

Table 1 Chemical composition of UHS-DP1000 steel (wt.%)

C	Si	Mn	Cr	Al	P	S	Fe
0.16	0.6	2.02	0.45	0.066	0.009	0.007	Balance

consisting of ferrite matrix (F) and martensite particles (M). This coexistence makes the material obtain an excellent combination of ductility and ultimate tensile strength.

3.2 Mechanical properties at different strain rates

Figure 2 shows the engineering stress–strain and true stress–strain curves of UHS-DP1000 steel at different strain rates. The variations in R_m, R_e, uniform elongation (A_u) and fracture elongation (A_f) with strain rates are illustrated in Fig. 3. As shown in Fig. 2, it is apparent that the steel presents a continuous yielding behavior irrespective of strain rate. In addition, at the stage of elastic deformation, the stress–strain curves at different strain rates are almost coincident with each other, and the stress increases rapidly with the strain. At the stage of plastic deformation, however, the tensile properties increase with increasing strain rate, which is also observed in Fig. 3a.

According to Fig. 3a, the average R_e and R_m increase moderately as the strain rate increases from 10^{-4} to 10^{1} s^{-1}. Thereafter, a sharp increase occurs until the strain rate reaches 10^{3} s^{-1}. In Fig. 3b, it can be found that as the strain rate increases from 10^{-4} to 0.5 s^{-1}, the average A_f increases and the average A_u decreases slowly until achieving a minimum of 9.63%. When the strain rates are in the range of 0.5−500 s^{-1}, both the average A_f and A_u increase, achieving the maxima of 24.25% and 16.77%, respectively. Then, they drop dramatically over the strain rate ranging from 500 to 10^{3} s^{-1}. This variation trend is different from the earlier reports in Refs. [15, 16].

3.3 Strain hardening behavior

The strain hardening behavior of metals has been extensively described by mathematical expression, because this allows the plastic deformation part of the true stress–strain curves to be treated by considering certain parameters that can be applied to study the formability and deformation mechanisms [17–19]. The Hollomon analysis has been widely applied to metals and alloys [20, 21]. Nevertheless, Ramos et al. [22] found that the Hollomon equation could not adequately describe the deformation of DP steels. Therefore, in this study, in order to deepen the understanding of the strain hardening behavior of UHS-DP1000 steel, the modified Crussard-Jaoul analysis based on the Swift equation [23] was used to determine strain hardening stages, which can be expressed as follows:

$$\ln\left(\frac{d\sigma}{d\varepsilon}\right) = (1-m)\ln\sigma - \ln(Cm) \quad (1)$$

where σ is the true stress, corresponding to the true strain ε; m is the strain hardening exponent; and C is the material constant.

The modified C-J plot of UHS-DP1000 steel at different strain rates is shown in Fig. 4. It can be observed that there are two different slopes at each strain rate for the steel, indicating that the steel has two distinct strain hardening regions, marked as Stage I and Stage II, where ε_{tr} denotes the transition strain between Stage I and Stage II; here, ε_{tr} represents a transition from elastic-to-plastic deformation of the martensite. As reported by Mazaheri et al. [7], the occurrence of different strain hardening stages in DP steels is related to different activated deformation mechanisms at the strain range corresponding to each stage. According to Eq. (1), the slope of the $\ln(d\sigma/d\varepsilon)$ vs. $\ln\sigma$ curve is given by $(1-m)$. In Fig. 4, regardless of the deformation rate, Stage I (lower strain level) has a larger slope $(1-m)$ compared with Stage II (higher strain level), indicating that the strain hardening behavior in Stage I is stronger than that in Stage II. The strong strain hardening behavior is related to a great number of dislocations piled up at the ferrite/martensite interfaces. However, the variety of $(1-m)$

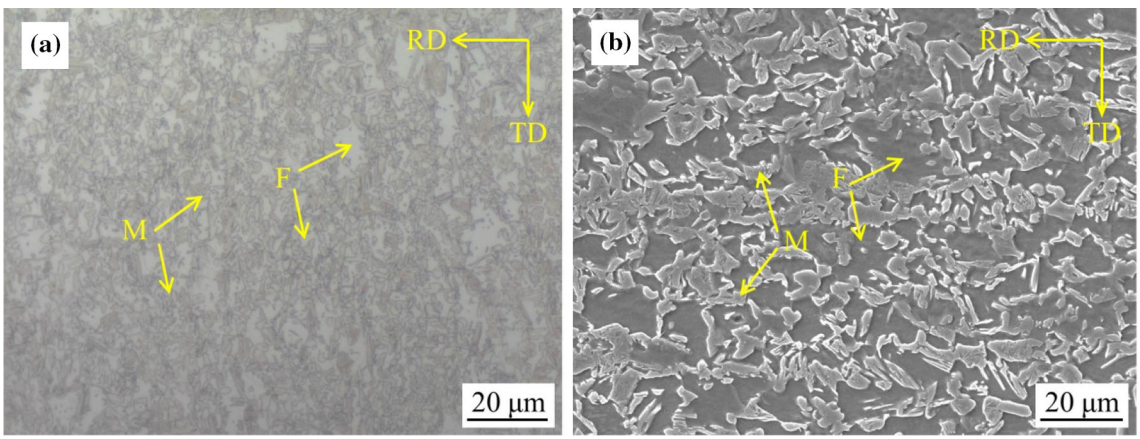

Fig. 1 Initial microstructure of UHS-DP1000 steel studied. **a** OM micrograph; **b** SEM micrograph. *RD* rolling direction; *TD* transverse direction

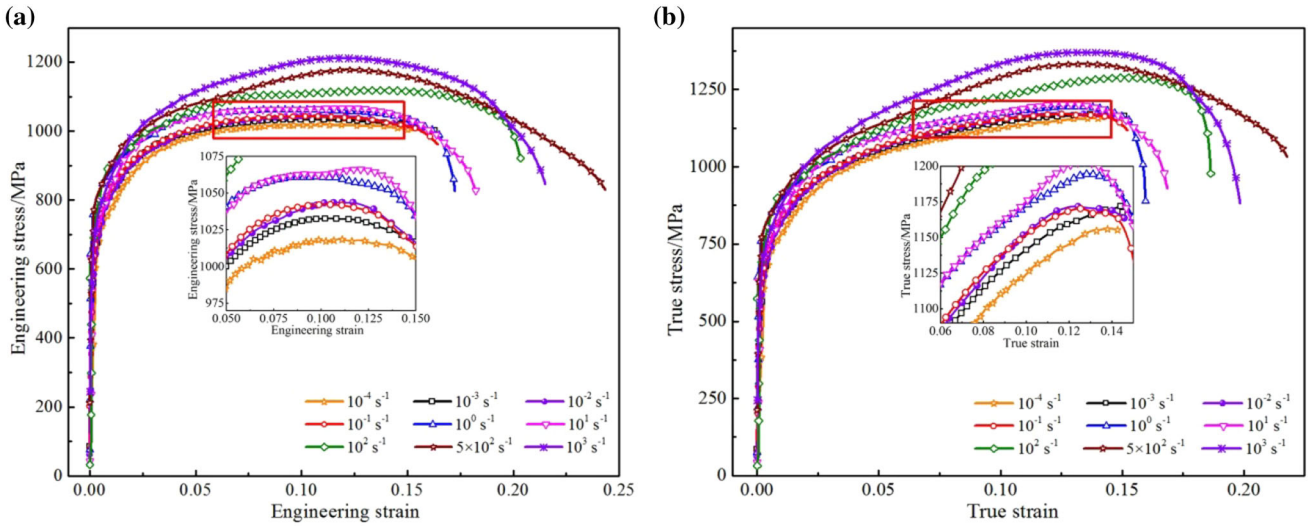

Fig. 2 Stress–strain curves of UHS-DP1000 steel at different strain rates. **a** Engineering stress–strain curves; **b** true stress–strain curves

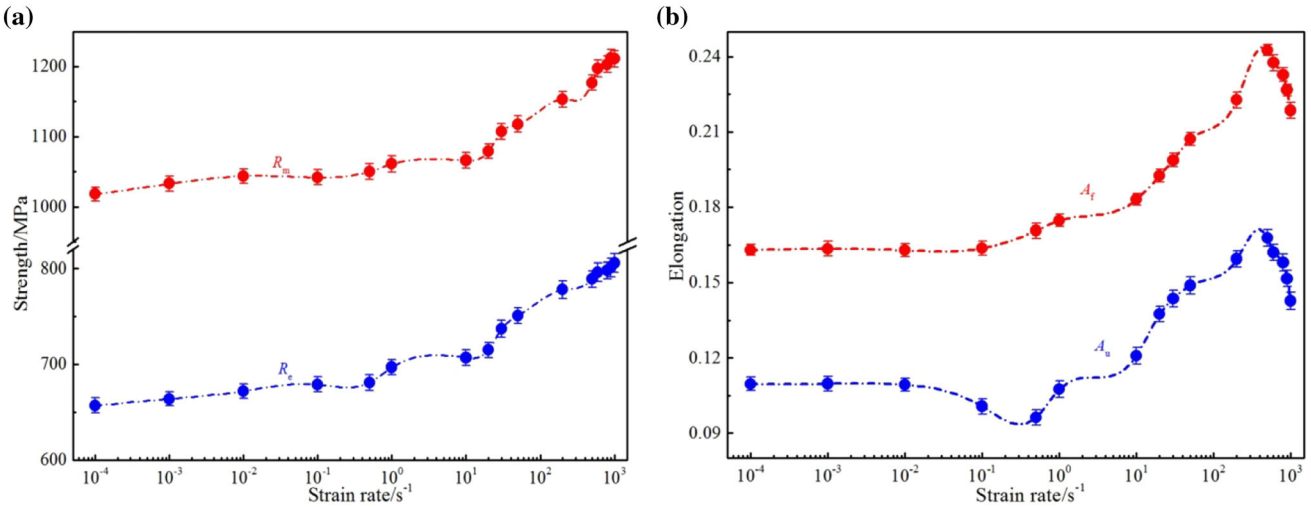

Fig. 3 Comprehensive mechanical properties of UHS-DP1000 steel at different strain rates. **a** Ultimate tensile strength and yield strength versus strain rate; **b** elongation versus strain rate

at the same deformation rate indicates the initiation of martensite plastic deformation [8, 24, 25]. This is because the pileup of dislocations results in yielding of martensite, and martensite has to deform plastically to accommodate the strain hardening of ferrite.

The values of $(1 - m)$ in two stages and ε_{tr} are summarized in Table 2. In Table 2, m_1 and m_2 are the strain hardening exponents based on the Swift equation. As seen in Fig. 4 and Table 2, in Stage I, the value of the slope $(1-m_1)$ increases from -7.853 to -3.589 with increasing strain rate, and m_1 decreases from 8.853 to 4.589. It is suggested that the strain hardening behavior of the steel increases as the strain rate increases. However, in Stage II, as the strain rate increases, the value of the slope $(1-m_2)$ decreases from -13.484 to -17.624 and m_2 increases from 14.484 to 18.624. This implies that the strain hardening behavior fades down with increasing strain rate in Stage II. Another significant phenomenon can be accessed from Fig. 4, and Table 2 shows that ε_{tr} becomes smaller with increasing strain rate, indicating that the plastic deformation of martensite starts earlier at a high strain rate than at a low strain rate [25].

To further interpret the strain hardening behavior, TEM analysis is performed. Figure 5 presents TEM images of the UHS-DP1000 steel at different strain rates. It can be confirmed that the dislocation density in ferrite close to the martensite/ferrite interfaces increases with increasing strain rate and martensite laths are elongated. Before deformation, the microstructure in Fig. 5a exhibits blocky martensite laths and a lower dislocation density in the

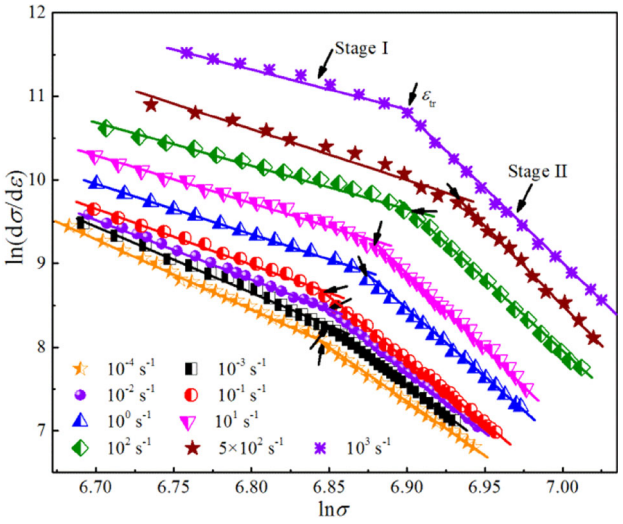

Fig. 4 Modified C–J plot of ln(dσ/dε) versus lnσ of UHS-DP1000 steel at different strain rates

Table 2 Summary of parameters related to strain hardening behavior of UHS-DP1000 steel at different strain rates

Strain rate/s^{-1}	Stage I		Stage II		ε_{tr}/%
	$1-m_1$	m_1	$1-m_2$	m_2	
10^{-4}	− 8.356	9.356	− 12.681	13.681	2.94
10^{-3}	− 7.853	8.853	− 13.484	14.484	2.73
10^{-2}	− 7.297	8.297	− 14.809	15.809	2.63
10^{-1}	− 6.686	7.686	− 14.861	15.861	2.57
10^{0}	− 5.926	6.926	− 15.883	16.883	2.38
10^{1}	− 5.256	6.256	− 16.202	17.202	2.27
10^{2}	− 4.634	5.634	− 16.918	17.918	2.10
5×10^{2}	− 4.394	5.394	− 17.391	18.391	2.01
10^{3}	− 3.589	4.589	− 17.624	18.624	1.92

vicinity of martensite. At a strain rate of 10^{-3} s^{-1} (Fig. 5b), the dislocations pile up near the martensite/ferrite interfaces and dislocation cells generate in ferrite grains. Similar dislocation cell formation is also observed at a strain rate of 10^{1} s^{-1} (Fig. 5c) and the dislocation density increases as the strain rate increases from 10^{-3} to 10^{1} s^{-1}, leading to an increase in strain hardening behavior of ferrite. Consequently, the plastic deformation energy difference between ferrite matrix and the martensite/ferrite interface could result in increasing in the ability of inhomogeneous plastic deformation, and the initiation and propagation of microvoids would be retarded at martensite/ferrite interface [26]. The uniform elongation decreases and fracture elongation increases for UHS-DP1000 steel (Fig. 3b). When the strain rate reaches 5×10^{2} s^{-1} (Fig. 5d), the amount of mobile dislocation increases [27, 28], leading to an increase in the plastic deformation ability of the steel. In addition, the dislocation motion resistance and degree of dislocation tangles also increase, resulting in an increase in strength. Another phenomenon observed in Fig. 5d is that the martensite lath is elongated. The main reason for this phenomenon is that numerous dislocations would generate at the vicinity of the martensite/ferrite interfaces and cause the martensite to yield earlier and deform plastically to accommodate the strain hardening of ferrite. This explains why the plastic deformation of martensite starts earlier with increasing strain rate (Fig. 4).

Previous studies have revealed that deformation process under a high strain rate is an adiabatic or quasi-adiabatic one. That is, the deformation energy of the specimen cannot immediately diffuse into the atmosphere, leading to an increase in the local temperature. The adiabatic heating temperature (ΔT) could be estimated by the following equation [29]:

$$\Delta T = \frac{h}{\rho c} \int \sigma \mathrm{d}\varepsilon \tag{2}$$

where h is the fraction of deformation work converting to thermal energy, $h = 0.9$; ρ is the density of steel, $\rho = 7.8$ g cm^{-3}; and c is the heat capacity of steel, $c = 0.46$ kJ kg^{-1} K^{-1}. Integrating the true stress–true strain curves and applying Eq. (2), ΔT of UHS-DP1000 steel at each strain rate was estimated and is given in Table 3. When the strain rate is higher than 5×10^{2} s^{-1}, the value of ΔT is above 60 °C, together with the deformation localization, resulting in more adiabatic heating temperature near the martensite/ferrite interfaces. The localized heating would result in increased dislocation mobility and enhanced deformation capacity of the steel.

With further increasing strain rate (Fig. 5e), the dislocation clustering and entanglement become more intense. The hardening degree caused by dislocation motion resistance has not been offset by softening, owing to mobile dislocation and adiabatic heating, leading to early void formation in the martensite, and the plastic deformation ability decreases.

3.4 Fracture mechanisms

With the aim of elucidating the effect of strain rate on the fracture mechanism of UHS-DP1000 steel, the fracture morphologies as well as deformed microstructures close to the fracture surface were studied at different deformation rates. The representative fracture morphologies of the tensile specimens are illustrated in Fig. 6.

At a low strain rate (10^{-3} s^{-1}), the fracture surface is covered with a large number of nonuniformly sized dimples and a few cleavage planes (Fig. 6a). This mixed

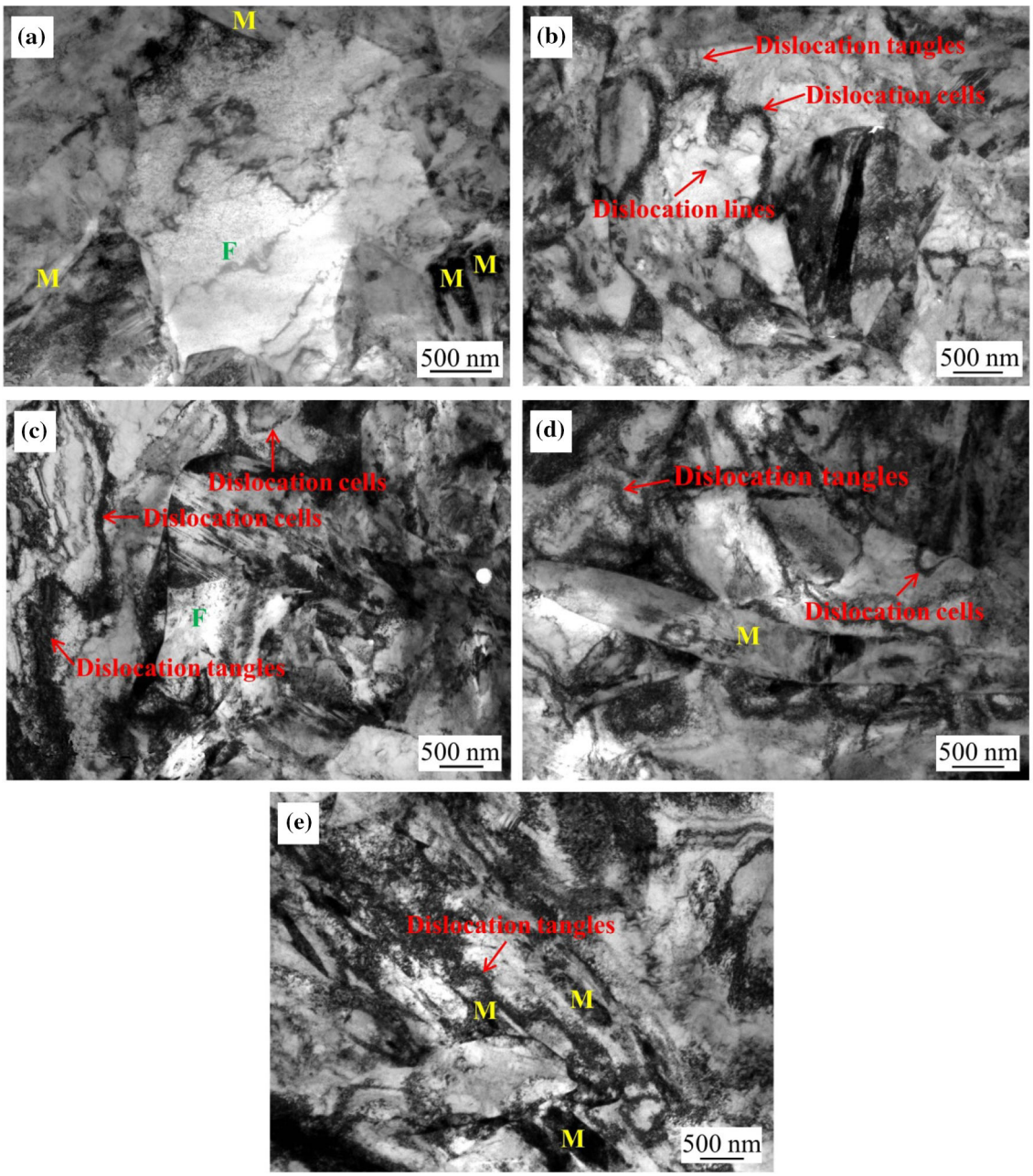

Fig. 5 TEM images of experimental UHS-DP1000 steel at various strain rates. **a** Before deformation; **b** 10^{-3} s^{-1}; **c** 10^{1} s^{-1}; **d** 5×10^{2} s^{-1}; **e** 10^{3} s^{-1}

Table 3 Adiabatic heating temperature under different deformation rates

Strain rate/s^{-1}	10^{-4}	10^{-3}	10^{-2}	10^{-1}	10^{0}	10^{1}	10^{2}	5×10^{2}	10^{3}
ΔT/°C	36.87	40.04	38.67	40.74	43.82	45.90	54.31	65.06	60.47

feature of dimple rupture and cleavage is usually called quasi-cleavage fracture. These cleavage facets are surrounded by small and shallow dimples. In addition, some deep dimples could also be observed. Mazaheri et al. [7] reported that the formation of these deep dimples was attributed to the voids formed at first in the

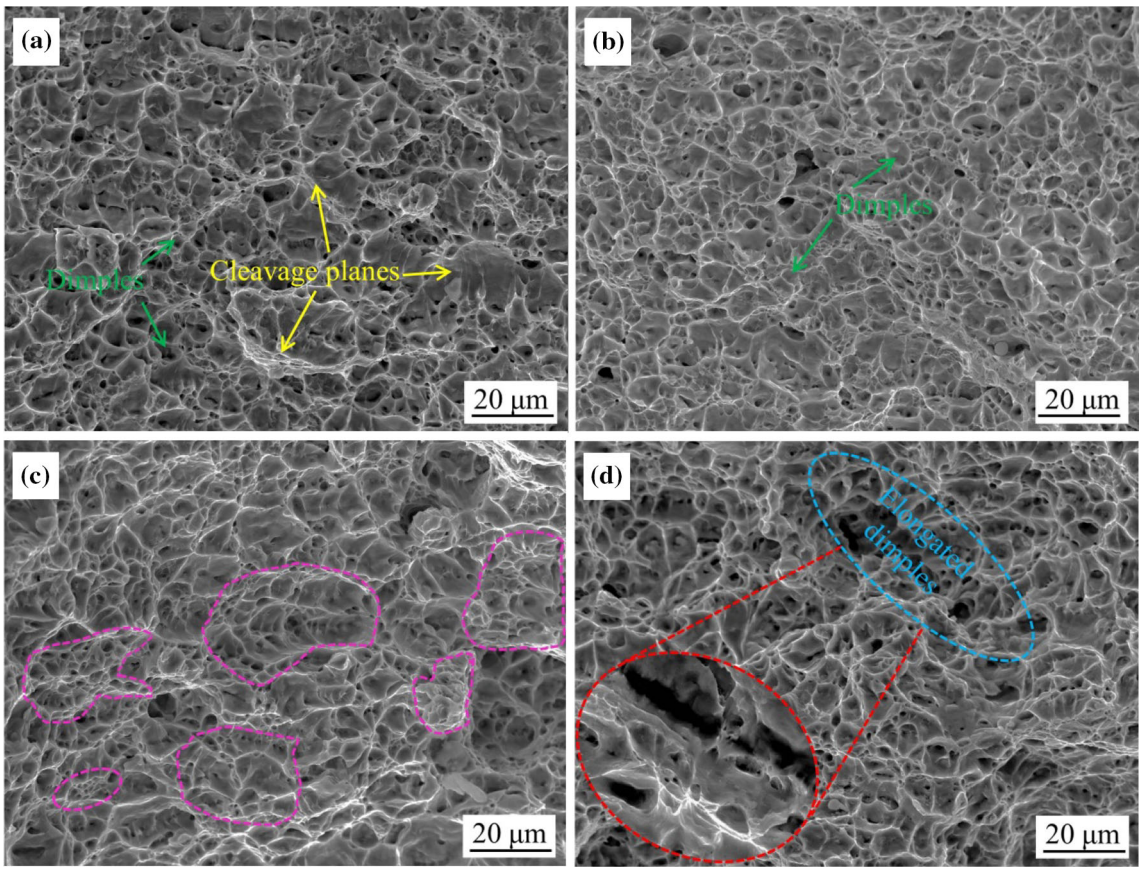

Fig. 6 Fracture morphologies of experimental UHS-DP1000 steel at different deformation rates. **a** 10^{-3} s^{-1}; **b** 10^{1} s^{-1}; **c** 5×10^{2} s^{-1}; **d** 10^{3} s^{-1}

martensite/ferrite interfaces, and these voids could grow with the strain in the tensile direction. With the increase in strain rate, as shown in Fig. 6b, c, the fracture surface consists of many more uniformly sized dimples in comparison with the deformed sample at 10^{-3} s^{-1}. It can also be seen that the dimples are much smaller and deeper at 5×10^{2} s^{-1} than at 10^{1} s^{-1}. Another phenomenon could be seen, whereby many small dimples are distributed on deep dimples. These results corroborate the fact that elongation at 5×10^{2} s^{-1} is more than that at 10^{1} s^{-1}. This is also consistent with the measured tensile results. The formation of the smaller and deeper dimples might be attributable to martensite yield, because of the increase in dislocation density close to the martensite/ferrite interfaces and adiabatic heating [30]. When the strain rate increases to 10^{3} s^{-1}, some areas consist of elongated and nonuniform dimples (Fig. 6d). According to Zhao et al. [6], these elongated dimples are an indication of large initial voids created by the fragmentation of blocky martensite laths. Based on previous studies [31–33], void nucleation, growth, and coalescence would result in fracture in DP steel. In order to provide further insight into the nascent or embryonic sites of voids, the microstructure close to the fracture surface of UHS-DP1000 steel at different deformation rates was examined. Figure 7 shows the void distribution close to the fracture surface at 10^{-3}, 10^{1}, 5×10^{2} and 10^{3} s^{-1}.

As noted in Fig. 7, it is observed that the fracture sample contained a large number of voids at different strain rates. The voids are more densely distributed closer to fracture surface and they display a variation in size and shape. Some voids are also elongated along the tensile direction. These results demonstrate that the void forms and grows with strain. In Fig. 7a, b, the voids are mainly located between martensite particles and the size in the tensile direction is small. Based on previous results [33], these voids occur in the ferrite particles, corresponding to void initiation at the martensite/ferrite interfaces close to the end martensite particle because of the incompatibility of plastic deformation. The martensite/ferrite interface decohesion and microvoid formation at low strain rates would lead to a decrease in the average A_u (Fig. 3b). In Fig. 7c, these voids and martensite particles elongated in the tensile direction are observed. Combined with the modified C-J analysis (Fig. 4), this is explained by the fact that with increasing strain rate, the martensite deformation starts earlier. This indicates that the void initiation would be diminished owing to plastic deformation of martensite at the

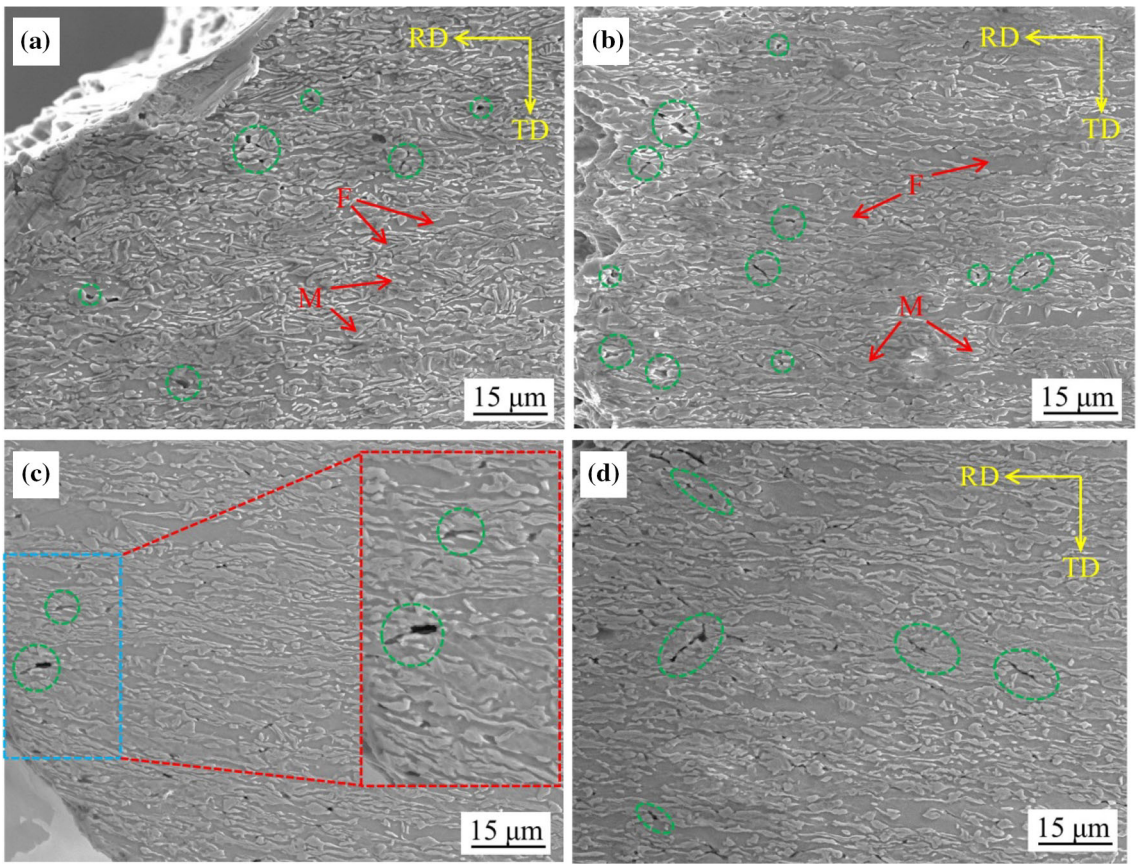

Fig. 7 SEM micrographs of microvoids close to fracture surface of experimental UHS-DP1000 steel at different deformation rates. **a** 10^{-3} s^{-1}; **b** 10^{1} s^{-1}; **c** 5×10^{2} s^{-1}; **d** 10^{3} s^{-1}

martensite/ferrite interfaces and the voids that initiate would grow to a larger size with increasing strain rate. In addition, adiabatic heating also plays an important role in increasing the void size. As a result, the void size at 5×10^{2} s^{-1} is much larger than that at 10^{1} s^{-1} and the elongation is also higher. As the strain rate increases further (Fig. 7d), it is also observed that some voids have passed through the martensite particle. Azuma et al. [34] reported that the voids tended to form at the concave side of martensite particles and propagated nearly perpendicular to the martensite lath, resulting in the fragmentation of the martensite particles (Fig. 5e). The width of these voids is almost equal to the thickness of the martensite particles after fracture.

4 Conclusions

1. Both R_e and R_m increase as the strain rate increases from 10^{-4} to 10^{3} s^{-1}. However, in the range of 10^{-4}–0.5 s^{-1}, A_f increases whereas A_u decreases slowly. Both A_f and A_u increase until the strain rate reaches 500 s^{-1} and then decreases dramatically.
2. With increasing strain rate, the dislocation density in ferrite increases and dislocation cells are generated in the ferrite grains. When the strain rate is 10^{3} s^{-1}, martensite fragmentation is observed.
3. Two types of voids have been observed near the fracture surface of UHS-DP1000 steel after tensile test at different strain rates. One type occurs in the ferrite particles and initiates at the martensite/ferrite interface close to the end martensite particle. The other is located in the martensite particles and initiates at the concave side of the martensite particles.

Acknowledgements The authors would like to acknowledge the financial support of the National Key R&D Program of China (Grant No. 2017YFB0304404) and Shandong Provincial Natural Science Foundation of China (Grant No. ZR2018MEM007).

References

[1] S. Huang, Y.X. Zhao, C.F. He, J. Iron Steel Res. Int. 21 (2014) 938–944.
[2] T.T. Huang, R.B. Gou, W.J. Dan, W.G. Zhang, Mater. Sci. Eng. A 672 (2016) 88–97.

[3] X.L. Ji, J.Y. Wang, C.C. Ji, J.H. Zhao, J. Iron Steel Res. Int. 22 (2015) 317–323.
[4] H. Ghassemi-Armaki, R. Maaß, S.P. Bhat, S. Sriram, J.R. Greer, K.S. Kumar, Acta Mater. 62 (2014) 197–211.
[5] G. Toktas, A. Toktas, A.D. Karaoglan, J. Iron Steel Res. Int. 21 (2014) 715–722.
[6] Z.Z. Zhao, T.T. Tong, J.H. Liang, H.X. Yin, A.M. Zhao, D. Tang, Mater. Sci. Eng. A 618 (2014) 182–188.
[7] Y. Mazaheri, A. Kermanpur, A. Najafizadeh, Mater. Sci. Eng. A 619 (2014) 1–11.
[8] M.P. Rao, V.S. Sarma, S. Sankaran, Metall. Mater. Trans. A 48 (2017) 1176–1188.
[9] Y. Tomita, K. Okabayashi, Metall. Trans. A 16 (1985) 865–872.
[10] N.D. Beynon, T.B. Jones, G. Fourlaris, Mater. Sci. Technol. 21 (2005) 103–112.
[11] S. Curtze, V.T. Kuokkala, M. Hokka, P. Peura, Mater. Sci. Eng. A 507 (2009) 124–131.
[12] H.J. Cai, H.J. Fan, R.B. Song, Q.F. Dai, Chin. J. Eng. 52 (2016) No. 2, 213–222.
[13] H.D. Yu, Y.J. Guo, X.M. Lai, Mater. Des. 30 (2009) 2501–2505.
[14] S. Oliver, T.B. Jones, G. Fourlaris, Mater. Sci. Technol. 23 (2007) 423–431.
[15] Q.F. Dai, R.B. Song, W.Y. Fan, Z.F. Guo, X.X. Guan, Acta Metall. Sin. 48 (2012) 1160–1165.
[16] Y. Gao, X. Chao, Z. He, Y.L. He, L. Li, J. Iron Steel Res. Int. 22 (2015) 48–54.
[17] G.C. Soares, B.M. Gonzalez, L. de Arruda Santos, Mater. Sci. Eng. A 684 (2017) 577–585.
[18] B.K. Jha, R. Avtar, V.S. Dwivedi, V. Ramaswany, J. Mater. Sci. Lett. 6 (1987) 891–893.
[19] S.O. Gashti, A. Fattah-Alhosseini, Y. Mazaheri, M.K. Keshavarz, J. Alloy. Compd. 658 (2016) 854–861.
[20] S. Vafaeian, A. Fattah-Alhosseini, Y. Mazaheri, M.K. Keshavarz, Mater. Sci. Eng. A 669 (2016) 480–489.
[21] H. Ashrafi, M. Shamanian, R. Emadi, N. Saeidi, Trans. Indian Inst. Met. 70 (2017) 1575–1584.
[22] L.F. Ramos, D.K. Matlock, G. Krauss, Metall. Trans. A 10 (1979) 259–261.
[23] H.W. Swift, J. Mech. Phys. Solids 1 (1952) 1–18.
[24] D. Das, P.P. Chattopadhyay, J. Mater. Sci. 44 (2009) 2957–2965.
[25] Y.G. Ko, C.W. Lee, S. Namgung, D.H. Shin, J. Alloy. Compd. 504 (2010) S452–S455.
[26] T. Matsuno, C. Teodosiu, D. Maeda, A. Uenishi, Int. J. Plast. 74 (2015) 17–34.
[27] R. Kapoor, S. Nemat-Nasser, Metall. Mater. Trans. A 31 (2000) 815–823.
[28] W.G. Johnston, J.J. Gilman, J. Appl. Phys. 30 (1959) 129–144.
[29] S. Curtze, V.T. Kuokkala, Matéria (Rio de Janeiro) 15 (2010) 157–163.
[30] D.Y. Dong, Y. Liu, Y.L. Yang, M. Ma, T. Jiang, Mater. Sci. Eng. A 594 (2014) 17–25.
[31] G.P. Potirniche, M.F. Horstemeyer, G.J. Wagner, P.M. Gullett, Int. J. Plast. 22 (2006) 257–278.
[32] G. Avramovic-Cingara, C.A.R. Saleh, M.K. Jain, D.S. Wilkinson, Metall. Mater. Trans. A 40 (2009) 3117–3127.
[33] M. Azuma, Structural control of void formation in dual phase steels, Technical University of Denmark, Lyngby, 2013.
[34] M. Azuma, S. Goutianos, N. Hansen, G. Winther, X. Huang, Mater. Sci. Technol. 28 (2012) 1092–1100.